Coherent control of topological states in an integrated waveguide lattice: Supporting Information

Alexey O. Mikhin,[†,‡] Viktoriia Rutckaia,[¶,§,‡] Roman S. Savelev,[†,‡] Ivan S. Sinev,[†] Andrea Alù,[¶,‖] and Maxim A. Gorlach[*,†]

†*School of Physics and Engineering, ITMO University, Saint Petersburg 197101, Russia*

‡*Authors who contributed equally to this work*

¶*Photonics Initiative, Advanced Science Research Center, The City University of New York, New York 10031, USA*

§*Centre for Innovation Competence SiLi-nano, Martin-Luther-University, Halle-Wittenberg, 06120 Halle (Saale), Germany*

‖*Physics Program, Graduate Center, The City University of New York, New York 10016, USA*

E-mail: m.gorlach@metalab.ifmo.ru

Contents

A. Methods

Sample Preparation. Designed nanostructured waveguides were fabricated using standard CMOS-compatible techniques. A silicon on sapphire substrate with a 600 nm device layer was purchased from *Universitywafers*. The substrate was cleaned in an acetone ultrasonic bath followed by isopropanol rinse, 5 min O2 plasma descum, and 10 min hot plate degassing at $180°C$. 230 nm HSQ mask was spin-coated on the surface (60 s at 5000 rpm) and baked on a hot plate for 2 minutes at $85°C$. Resist was patterned using *JEOL* 100 KeV electron-beam lithography system with 1 nA current. To minimize the charging effect of the insulating substrate, a 10 nm conductive polymer layer (*Electra 92* from *Allresist*) was deposited on the surface before the lithography. After the exposure, the conductive polymer was removed using DI water, followed by a 2 min post-exposure bake at $195°C$. Resist was developed in TMAH (25%) for 70 s followed by 60 s DI water- and 20 s isopropanol-rinsing. The pattern was transferred to the Si slab using the ICP RIE (*Oxford PlasmaPro System 100 Cobra*) in HBr(20 sccm)/Ar(10 sccm) gas mixture for 2 min 30 s (ICP 1500 W, RF 40 W, pressure 8 mTorr). A subsequent buffered HF dip removed the residuals of the mask.

Third-harmonic spectroscopy. To image the propagation of the modes of the structured waveguide array, we excite the sample from the substrate side with a 10x Mitutoyo objective focusing the laser radiation on one of the grating couplers at a small incidence angle. Femtosecond laser pulses are provided by the optical parametric amplifier (Light Conversion Orpheus) pumped by 250 fs Yb laser (LightConversion Pharos) at a repetition rate of 1 MHz. The automated parametric ampification system allows us to tune the excitation wavelength within a broad spectral range. The area of the sample containing the directional coupler and the waveguide array was imaged on a CCD camera (PyLoN 400BR_eXcelon) with a

50x Mitutoyo objective. The residual scattered light at the fundamental laser frequency is blocked with a shortpass filter.

B. Tight binding description and topological properties

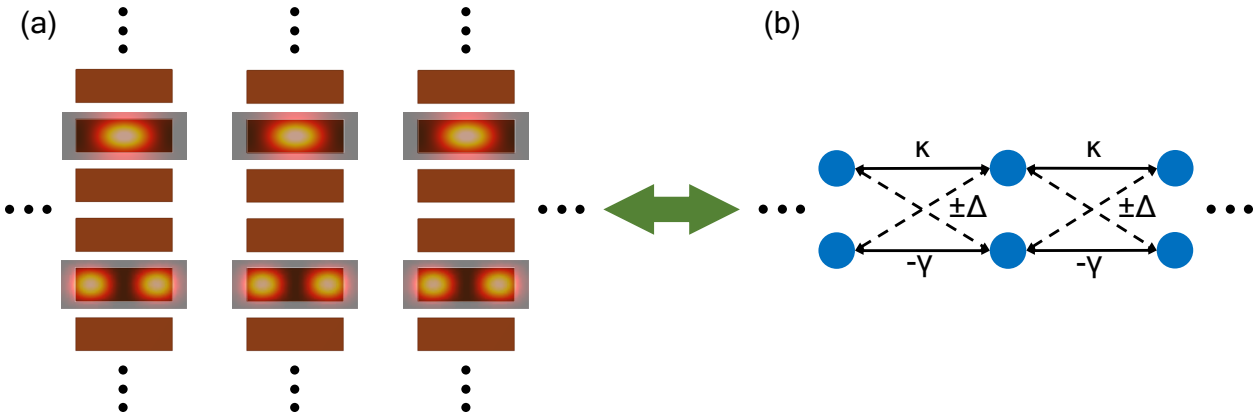

Figure S1: (a) Schematic of a one-dimensional array of periodic waveguides supporting two degenerate modes. (b) Equivalent representation of the waveguide array as a ladder with the doubled number of the sites (blue circles); arrows depict the coupling between the neighboring sites.

The physics of the designed one-dimensional array of multimode waveguides can be understood within the framework of the tight-binding model, assuming the evanescent coupling between the nearest-neighbor waveguides. We denote the amplitudes of the two degenerate modes in nth individual waveguide as $u_1^{(n)}$ and $u_2^{(n)}$, and vector $\mathbf{k}$ includes Bloch wave number k_x characterizing phase advance between the neighboring waveguides and the propagation constant k_z along the waveguide axis. Then the coupling matrices between the modes of the adjacent waveguides with the numbers n and $n+1$ can be written as:

$$\hat{\varkappa}_{n,n\pm1} = \begin{pmatrix} \varkappa & \pm\Delta \\ \mp\Delta & -\gamma \end{pmatrix}, \tag{S1}$$

where diagonal entries characterize the coupling between the modes of the same type, off-diagonal entries describe the coupling between the different types of modes, and the equality

of the non-diagonal components $\varkappa_{n,n\pm1}^{(12)} = \varkappa_{n,n\pm1}^{(21)}$ is ensured by the appropriate relative normalization of $u_1^{(n)}$ and $u_2^{(n)}$. Note that there is a degree of freedom related to the relative phase between the modes u_1 and u_2. For greater clarity and to avoid complex coupling constants, we define the phases of u_1 and u_2 differently compared to the original theoretical work Ref.[1], which does not affect our conclusions.

Denoting the propagation constants of a collective mode in the waveguide array and the mode in an individual waveguide as k_{z0} and k_z, respectively, we obtain the eigenvalue equation defining the spectrum $k_z(k_x)$ of the waveguide array as[1]:

$$\hat{H}(k) \begin{pmatrix} u_1 \\ \\ u_2 \end{pmatrix} = (k_z - k_{z0}) \begin{pmatrix} u_1 \\ \\ u_2 \end{pmatrix} , \tag{S2}$$

where Bloch Hamiltonian $\hat{H}(k_x)$ obtained from the coupling matrices Eq. (S1) and Bloch theorem reads

$$\hat{H}(k_x) = \begin{pmatrix} 2\varkappa \cos k_x & 2i\Delta \sin k_x \\ -2i\Delta \sin k_x & -2\gamma \cos k_x \end{pmatrix} . \tag{S3}$$

The spectrum of the Hamiltonian Eq. (S3) takes the form

$$k_z^{(\pm)} = k_{z0} + (\varkappa - \gamma) \cos k_x \pm \sqrt{(\varkappa + \gamma)^2 \cos^2 k_x + 4\Delta^2 \sin^2 k_x} , \tag{S4}$$

where k_x ranges from $-\pi$ to π. For $\varkappa$ and γ of different signs, a complete bandgap does not exist. However, it opens once $\varkappa$ and γ have the same sign. In such case, diagonalizing Bloch Hamiltonian, we retrieve the eigenvalues $k_z^{(\pm)}(k_x)$ and associated eigenfunctions $|\psi\rangle^{(\pm)} = (u_1(k_x), u_2(k_x))^T$. Focusing on the band below the bandgap, we evaluate the Zak phase defined as

$$\gamma_Z = i \int_{-\pi}^{\pi} \langle \psi \, | \partial_k \, \psi \rangle \, dk \, .$$

Straightforward calculation shows that the Zak phase equals π modulo 2π.

In the experimentally studied array of silicon waveguides the degeneracy of the modes

is not perfect, i.e. there is a detuning δk between the propagation constants. In terms of coupled-mode theory, this can be taken into account by modifying the eigenvalue equation as follows:

$$\hat{H}(k)\begin{pmatrix} u_1 \\ u_2 \end{pmatrix} = \begin{pmatrix} k_z - k_{z0} - \delta k/2 & 0 \\ 0 & k_z - k_{z0} + \delta k/2 \end{pmatrix}\begin{pmatrix} u_1 \\ u_2 \end{pmatrix}, \tag{S5}$$

where k_z is the propagation constant of the collective mode and $k_{z0} \pm \delta k/2$ are the propagation constants for the two non-degenerate modes in the individual waveguide. Similarly to the analysis above, we derive the spectrum of the propagation constants as a function of the Bloch momentum k_x. Inspecting the gap in this spectrum, we recover[1] that the critical value of detuning is equal to $\delta k = 2(\kappa+\gamma)$. When the detuning exceeds this threshold, the gap in the spectrum propagation constants reopens becoming topologically trivial. This implies that there is a limited spectral range, in which the system retains its topological properties and supports hybrid edge states. As it is discussed in the main text, for the realistic structures under study the operational wavelength range is approximately $50 - 100$ nm.

According to the bulk-boundary correspondence, nontrivial topological properties of the bands enable topological edge states. The mechanism of formation of the edge modes can be understood by considering two coupled waveguides. In this case the eigenvalues read:

$$\delta k_z^2 = \frac{\kappa^2 + \gamma^2}{2} + \Delta^2 \pm (\kappa + \gamma)\sqrt{\frac{(\kappa - \gamma)^2}{4} + \Delta^2}, \tag{S6}$$

which in the limiting case $\Delta = \kappa = \gamma$ simplifies to

$$\delta k_z = \begin{bmatrix} 0 \\ \pm 2\kappa \end{bmatrix}. \tag{S7}$$

The two degenerate eigenvectors corresponding to the zero eigenvalues are:

$$(u_1^{(1)}, u_2^{(1)}, u_1^{(2)}, u_2^{(2)})^T = \begin{bmatrix} (1,1,0,0)^T/\sqrt{2} \\ (0,0,1,-1)^T/\sqrt{2} \end{bmatrix}. \tag{S8}$$

This means that a specific combination of the two modes u_1 and u_2 excited in the edge waveguide is completely uncoupled from the neighbor waveguide.

A similar mechanism leads to the formation of the two edge modes with $\delta k_z = 0$ in the finite array with an arbitrary number of the waveguides. In the case of perfectly degenerate modes of the individual waveguide, the properties of the edge modes in a semi-infinite array can be found analytically for arbitrary coupling constants. The amplitudes of the modes in even waveguides turn out to be zero, while in the odd ones the dependence on the number is given by[1]:

$$\frac{u_1^{(2n+1)}}{u_1^{(2n-1)}} = \frac{u_2^{(2n+1)}}{u_2^{(2n-1)}} = \frac{1-\alpha}{1+\alpha}, \;\; u_1^{(2n)} = u_2^{(2n)} = 0, \tag{S9}$$

where $\alpha = \dfrac{\sqrt{\varkappa\gamma}}{\Delta}$, $n = 1, 2, \ldots$ The ratio between the amplitudes of the two modes in a given waveguide is determined by the ratio of the coupling constants:

$$\frac{u_1^{(2n-1)}}{u_2^{(2n-1)}} = \sqrt{\frac{\gamma}{\kappa}}, \tag{S10}$$

which is close to one in the experimental design.

C. Dispersion engineering of a multimode waveguide

In order to achieve the topological phase of the waveguide array, one needs to ensure that the modes of the neighboring waveguides interact with each other according to the coupling matrix Eq. (S1) with the same sign of the coupling constants κ and γ. This can be achieved if two quasi-degenerate modes of a waveguide possess different symmetry with respect to the vertical plane of symmetry. In our work, we have designed a silicon waveguide with the

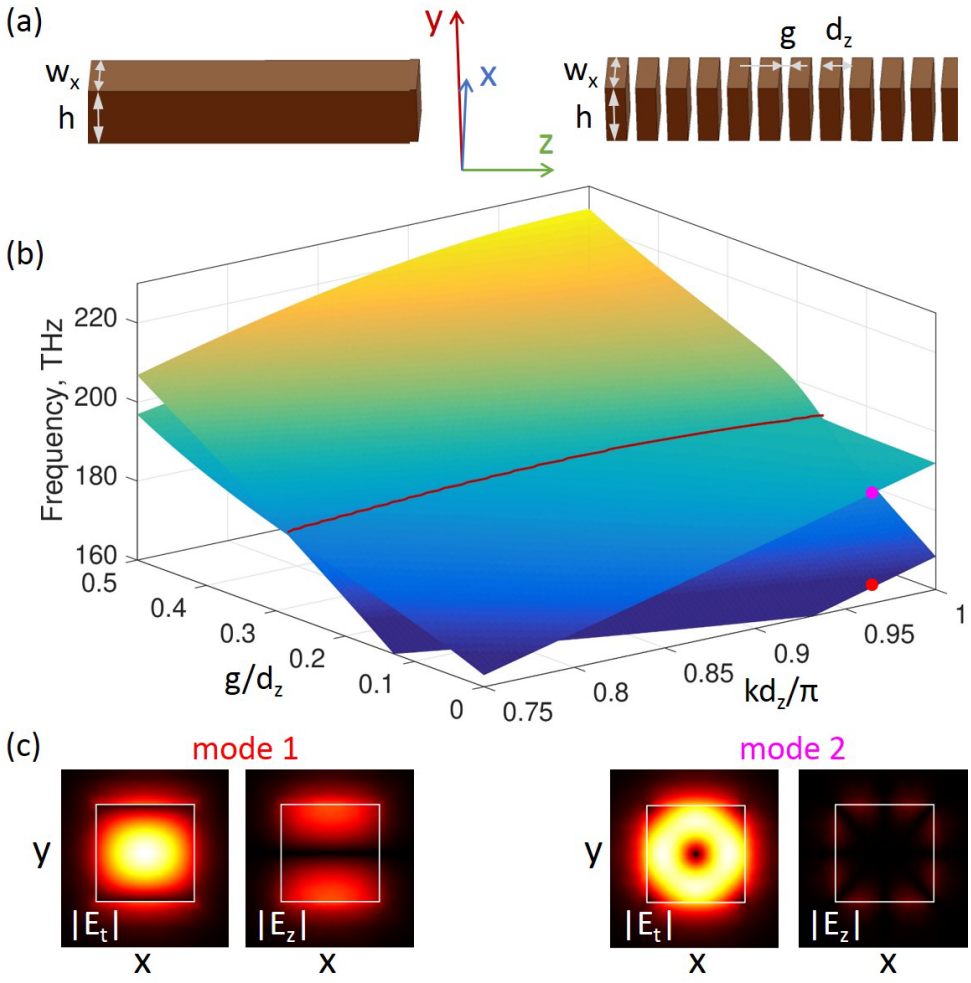

Figure S2: (a) Schematic of a rectangular homogeneous and periodic silicon waveguides. Parameters used in the calculations: $w_x = 605$ nm, $h = 600$ nm, $d_z = 300$ nm, $\varepsilon_{Si} = 12.25$. (b) Eigenfrequency of two modes of a silicon waveguide as a function of the normalized Bloch wavenumber kd_z/π and the size of the gap normalized by the period, g/d_z. Red line indicates intersection of the two surfaces. (c) Electric field (tangential E_t and normal E_z components) distributions in the Oxy plane for the modes marked with red (mode 1) and magenta (mode 2) circles in (b).

desired dispersion by introducing a modulation of the permittivity with a subwavelength period to an initially homogeneous rectangular waveguide. To illustrate this, we consider a rectangular silicon waveguide in vacuum, as schematically shown in Fig. S2(a). The symmetry requirements imply that quasi-degenerate modes should possess the same symmetry with respect to the plane $y = 0$ and different symmetry with respect to the plane $x = 0$.

The lowest frequency modes that satisfy such conditions are the first hybrid quasi-HE_{11} mode with dominant x (y) component of magnetic (electric) field and the first quasi-TE_{01} mode with dominant z (ϕ) component of magnetic (electric) field where ϕ is the azimuthal angle. In the homogeneous waveguide, these modes are well separated in frequency as shown in Fig. S2(b) for $g = 0$, where g is the gap width. The distribution of tangential and normal components of electric field for the first [red circle in Fig. S2(b)] and second [magenta circle in Fig. S2(b)] modes is shown in Fig. S2(c).

After introducing small gaps in the waveguide with a constant period, the frequencies of both modes start to grow in accordance with the perturbation theory[2]. However, the rates of frequency growth are different due to the different field distributions of these modes: the first mode of HE type possesses a non-zero z component of electric field, while for the second quasi-TE mode E_z is negligible. As a result, the dispersions of these mode intersect for the certain value of the gap. By tuning the size of the gap, it is possible to shift the intersection point almost to any value of the Bloch wavenumber, as shown in Fig. S2(b) by the red curve. Introduction of the low-index substrate slightly modifies the dispersion but does not change the outlined picture qualitatively.

According to the predictions of the theoretical model, the array of the designed waveguides possesses two edge states. The field distributions of 6 (out of 12) bulk states and one of the two edge states in the array of 7 waveguides are shown in Fig. S3(a,b), respectively. The field profile of the edge state illustrates two main points: strong localization of the field at the edge waveguides and strong asymmetry of the field distribution in the edge waveguides. Such asymmetry indicates hybrid nature of these modes. Indeed, the field profile of the edge mode represents a superposition of the modes of the individual waveguide with 0 or π phase difference as illustrated in Fig. S3(c). Here the phase of the individual modes was chosen based on the phase of the (dominant) y-component of the electric field on the line $y = z = 0$ passing through the center of the waveguide cross section. In this case, the ratio of the complex amplitudes of the modes in a single waveguide (S10) is real and either positive

(zero phase difference) or negative (π phase difference), which correspond to the edge state localized at the left or right edges of the array. The field distributions of the bulk modes in each of the waveguides are also asymmetric. However, the asymmetry is opposite to that of the edge modes, making field distributions of the bulk and edge modes quasi-orthogonal. Consequently, feeding the waveguide array by a proper superposition of the modes in the extended edge waveguide allows for selective switching between the excitation of the bulk and edge modes, as discussed in the next section.

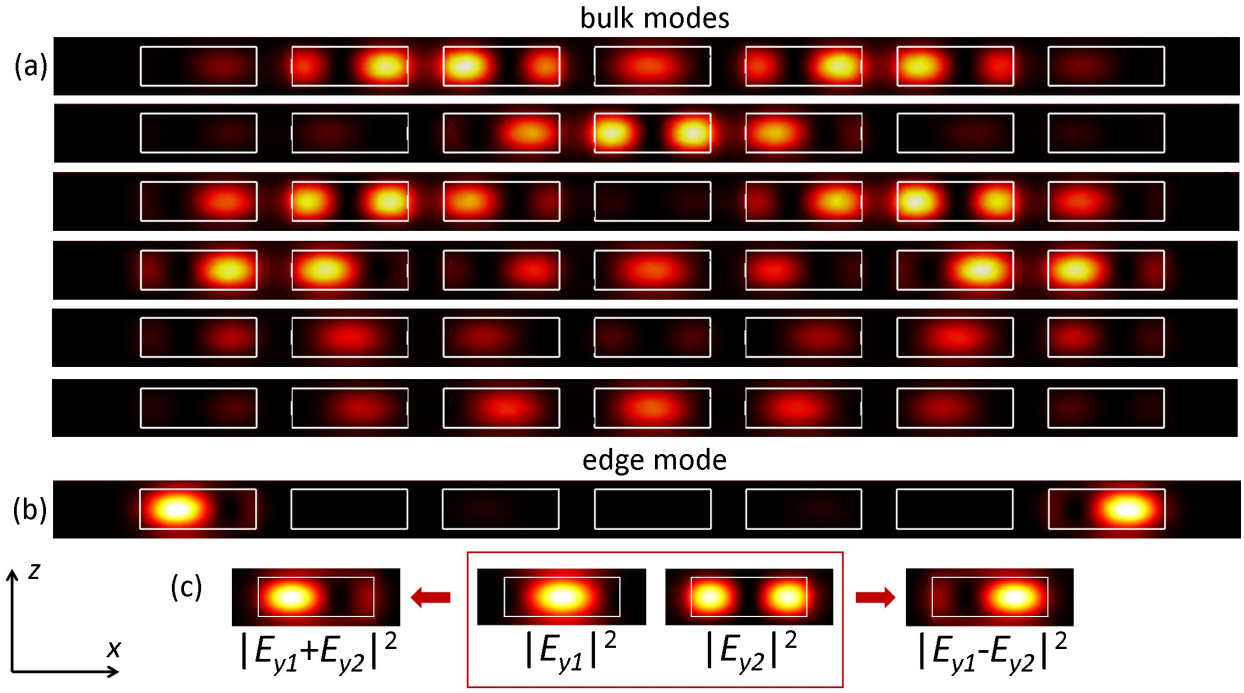

Figure S3: (a,b) Distribution of the squared amplitude of the y component of electric field $|E_y|^2$ for (a) 6 bulk modes and (b) one of the edge modes propagating in positive direction of z in the array of 7 waveguides; one unit cell along z axis is shown. The propagation constant of the modes corresponds to the intersection point of the two modes in the individual waveguide. (c) Field profiles of two modes of the individual waveguide $|E_{y1}|^2$, $|E_{y2}|^2$ and their superpositions.

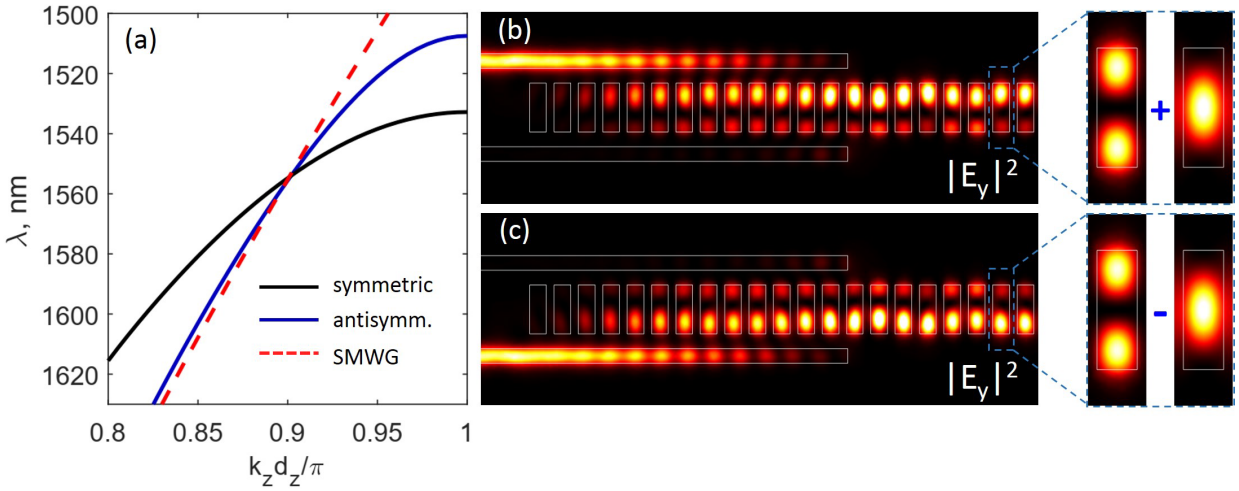

Figure S4: (a) Dispersion of symmetric (black curve), antisymmetric (blue curve) modes of the periodic waveguide and the mode of a single-mode waveguide (red dashed curve). (b,c) Electric field intensity distribution in a directional coupler in the plane parallel to the substrate under excitation through upper (b) and lower (c) single-mode waveguide.

D. Excitation of the edge modes of the waveguide array

Strong localization and asymmetry of the edge mode near field allow for its efficient selective excitation through the extended edge waveguide. For that purpose, one has to ensure the proper phase difference between two excited modes in the extended periodic waveguide. We have attained this by coupling the periodic waveguide to one of the homogeneous single-mode bus waveguides (SMWG), as shown in Fig. 4b of the main text. The width of the SMWG was adjusted in such a way that the dispersion of its fundamental mode crosses the intersection point of the two modes of the structured waveguide, see Fig. S4(a).

At the intersection frequency, the superposition of the modes of the periodic waveguide $|E_{y1} \pm E_{y2}|^2$ has vanishing field on the right/left side [Fig. S3(b)]. Consequently, $|E_{y1} \pm E_{y2}|^2$ wave couples only to the mode of the SMWG that is placed on the left/right side (with respect to the propagation direction) from the periodic one. The simulations of the directional coupler, Fig. S4(b,c), have shown that indeed depending on the position of the SMWG the power is transferred to the periodic waveguide with almost 100% efficiency in the form of either $\mathbf{E}_1 + \mathbf{E}_2$ or $\mathbf{E}_1 - \mathbf{E}_2$ wave. If such extended periodic waveguide is positioned on the

left side of the waveguide array, the $\mathbf{E}_1 + \mathbf{E}_2$ field corresponds to the edge mode, while the $\mathbf{E}_1 - \mathbf{E}_2$ field corresponds to the bulk modes. Thus, switching between two input SMWGs allows to switch between the excitation of the edge and bulk modes of the array.

In the experiments incident light was coupled into the SMWGs from the far-field by using a combination of a taper and a grating. Linear taper had the minimal width equal to the SMWG width, maximal width equal to 10 μm and apex angle equal to 6°. The grating parameters, bar width $w = 460$ nm and period $a = 570$ nm, were optimized for the excitation from the substrate at $\approx 9°$ angle. The part of the SMWGs between the directional coupler and the taper was bent at 15° to ensure enough space between the tapers.

E. Details on experimental data analysis

The field distributions depicted in Fig. 4 of the main text exhibit a noticeable decrease of the signal intensity with the z coordinate along the waveguides. Interpreting this data, one should keep in mind that the intensity of the third harmonic is proportional to the cube of intensity at the fundamental frequency. Therefore, if the measured third harmonic signal has an attenuation length of l, the fundamental wave decays at the distance equal to $3l$. Hence, the respective field profile at the fundamental frequency is much more homogeneous.

Since the absorption in silicon in the studied wavelength range is negligible, the observed decay of the edge modes should be attributed to the scattering of the signal on the defects in the waveguide structure. To determine the propagation length of the modes, we integrate the third harmonic signal over the edge of the waveguide structure and plot the dependence of this quantity on the propagation distance (Fig. S5). Here, the starting point (0 μm) corresponds to the distance 5 μm away from the edge of the waveguide array, which was chosen as a starting point for fitting to avoid the contribution of parasitic scattering at the entry point of the array. For the sake of comparison, both signals are normalized to their respective values at 0 μm. The obtained quantity is then fitted by the exponential formula.

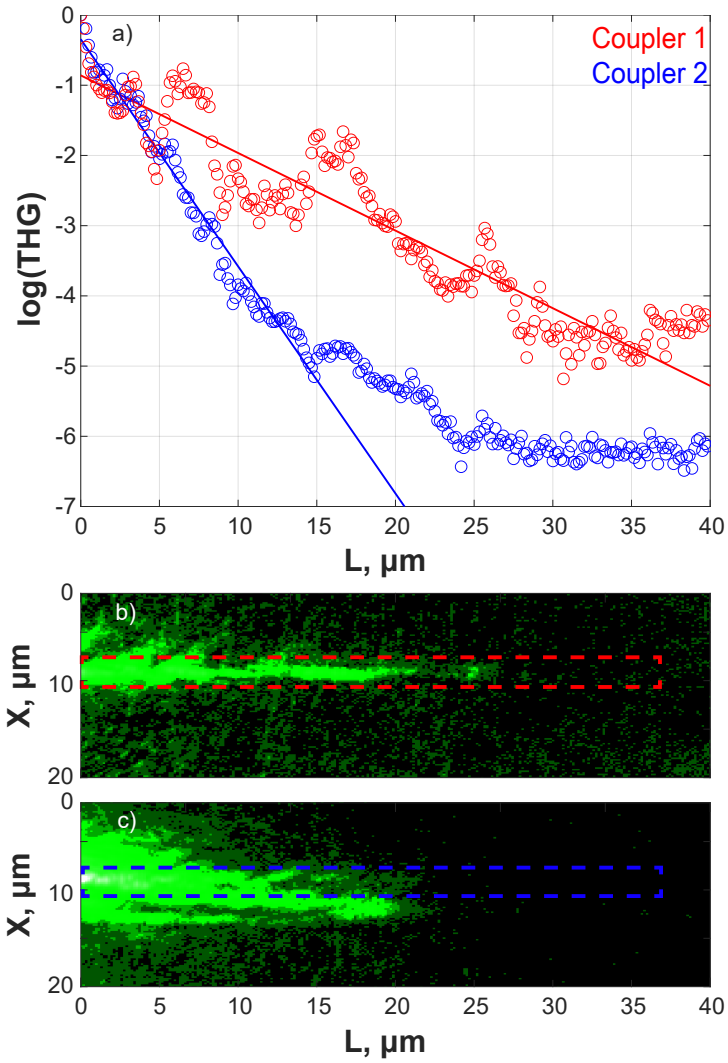

Figure S5: a) Integral third harmonic signal along the edge of the array of the structure presented in the main manuscrpit plotted in logarithmic scale for an excitation wavelength of 1560 μm. The area of integration is shown by a dashed line in panels b) and c) which show the THG images for excitation through coupler 1 and coupler 2, respectively. The integrated third harmonic signals were normalized to their respective values at 0 μm.

If the structure is excited through the coupler 1, light propagates via the edge mode with a typical attenuation length of the third harmonic signal equal to 9 μm (Fig. S5a, red color), which means that the propagation length of the fundamental mode is equal to 27 μm, which is comparable to the length of the structure (25 μm). Characteristic oscillations at the respective curve suggest the interference of the incident and reflected signals. Note that the topological properties of our setup are characterized by the one-dimensional invariant (Zak phase) and hence there is no topological protection against backscattering along the z axis.

If the structure is excited through the coupler 2, light diffracts into the bulk of the structure. Therefore, the decrease of the intensity at the edge is due to the combination of the two factors: (i) backreflection; (ii) diffraction of light in the bulk of the lattice. Accordingly, attenuation length of the third harmonic signal is less and is roughly 3.1 μm (Fig. S5a, blue curve), which yields the propagation length 9.3 μm at the fundamental frequency.

To better illustrate the switching between the excitation of bulk and edge modes, we provide Figure S6 which refers to the same experimental structure, but includes seven representative wavelengths that cover the entire wavelength range of interest. Here, in contrast with the Fig. 4 in the main manuscript, we disregard the actual spectral dependence of the total coupling efficiency by optimizing the color scale independently for each image. Examining the obtained field maps, we observe that the panels in the upper row (excitation through coupler 1) show the field distribution mostly pinned to the edge of the structures. At the same time, the panels in the lower row (excitation through coupler 2) depict the field distribution which clearly diffracts in the bulk of the array. Note also that the field distributions obtained at extreme wavelengths of 1500 and 1620 nm are much less clear which should be attributed to the drop in the efficiency of the couplers.

Furthermore, in Figure S7 we provide additional data to illustrate the transition to the trivial regime upon reaching the threshold value of the wavelength, when the detuning between the propagation constants of the two waveguide modes closes the bandgap. For that

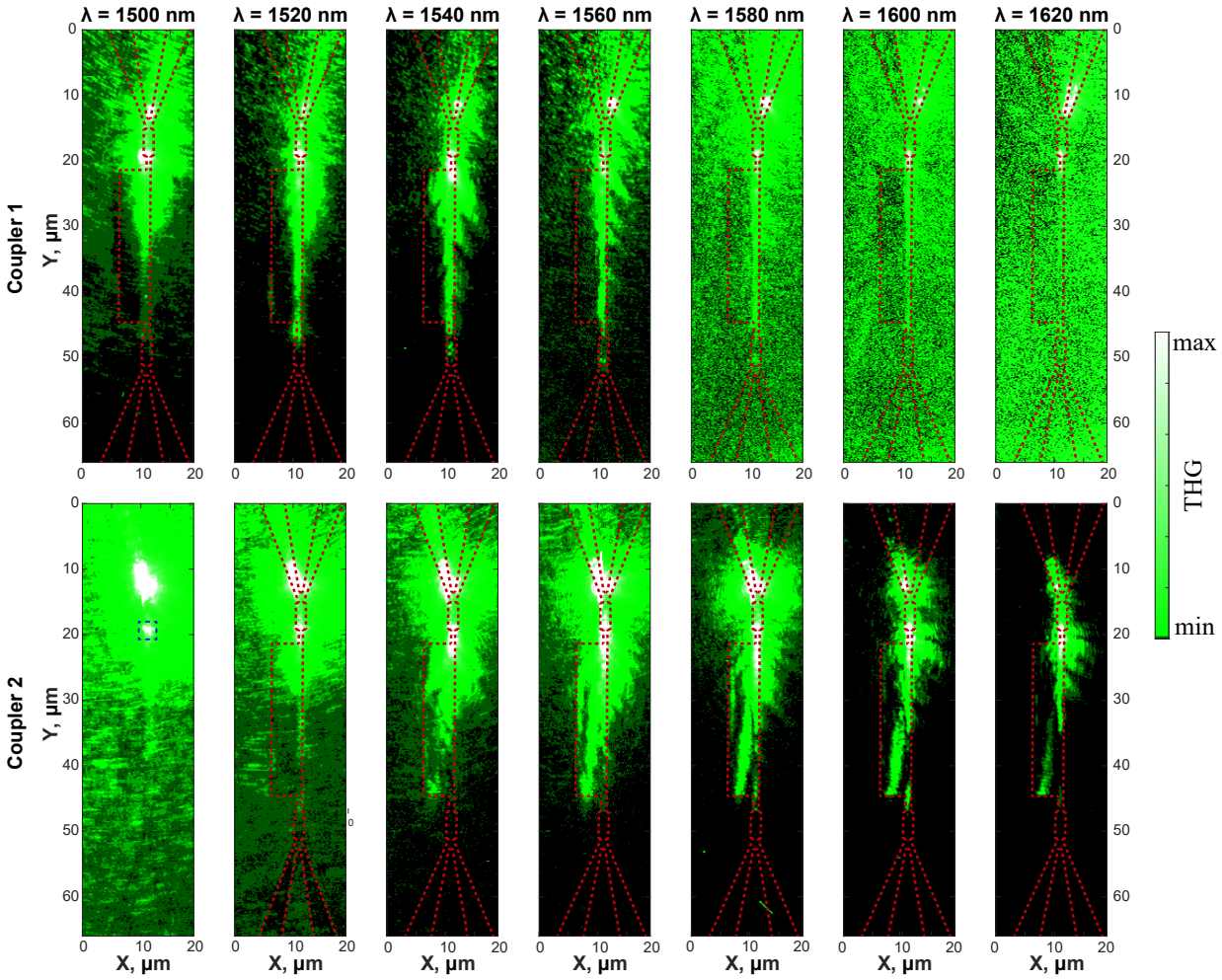

Figure S6: Propagation of topological edge modes and bulk modes in the waveguide array from the main manuscript (Fig. 4) for the different excitation wavelengths visualized via third harmonic spectroscopy. Third harmonic signal in each map is normalized to the signal at the point where the single-mode waveguide is coupled to the structured waveguide (shown by the dashed square in the panel corresponding to the 1500 nm, coupler 2). (Upper row) Excitation through coupler 1 (edge mode regime). (Lower row) Excitation through coupler 2 (bulk mode regime). Red dashed lines show the contours of the structure. The color scale is optimized independently for each image.

purpose, we use a different device compared to the one discussed in the manuscript main text and above. In this particular structure, the sizes of the elements are chosen such that the band of the directional coupler intersects the spectral region where the topological gap of the structured waveguide array is closed. In this case, when the wavelength is detuned far from the gap center, bulk modes are excited both for the excitation via coupler 2 and

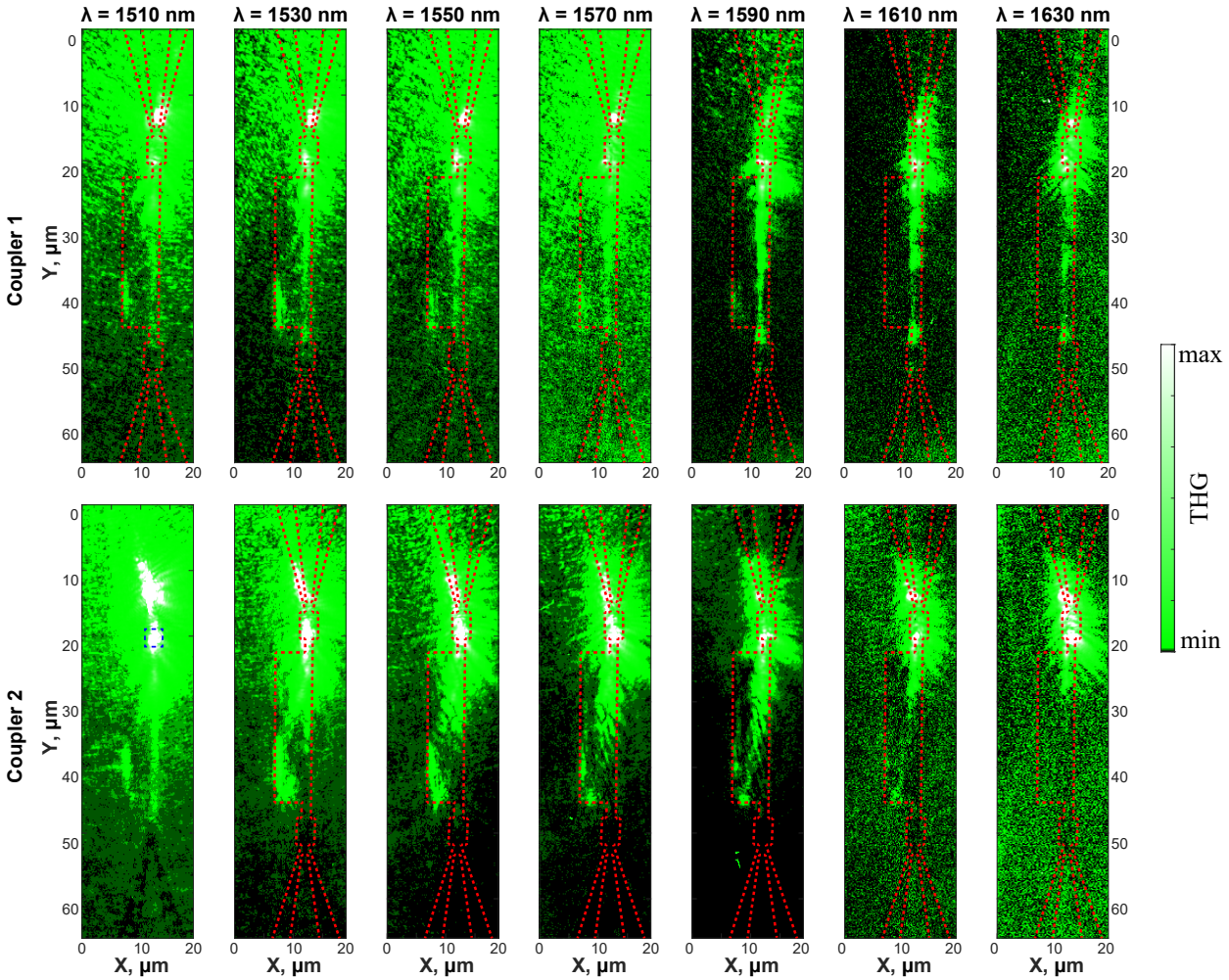

Figure S7: Propagation of topological edge modes and bulk modes in another experimental sample visualized via third harmonic signal for different excitation wavelengths. (Upper row) Excitation through coupler 1 (edge mode regime). (Lower row) Excitation through coupler 2 (bulk mode regime). Red dashed lines show the contours of the structure. Third harmonic signal in each map is normalized to the signal at the point where the single-mode waveguide is coupled to the structured waveguide (shown by the blue dashed square in panel corresponding to the wavelength 1510 nm coupler 2). The color scale is optimized independently for each image. Note, that the wavelength of the excitation is different from previous figures (on previous figures we consider the excitation wavelength from 1500 to 1620 nm).

coupler 1. Figure S7 shows the maps of the third harmonic signal obtained for this structure for both excitation configurations and different wavelengths. Here, at 1590 nm the structure demonstrates similar behaviour to the device discussed in the main text, with a pronounced edge mode for coupler 1 excitation and bulk mode for coupler 2 configuration. However, as

the wavelength decreases towards 1500 nm, both configurations demonstrate delocalization of the third harmonic signal in the array in agreement with the theoretical and numerical predictions.

References

(1) Savelev, R. S.; Gorlach, M. A. Topological states in arrays of optical waveguides engineered via mode interference. *Physical Review B* **2020**, *102*, 161112.

(2) Johnson, S. G.; Ibanescu, M.; Skorobogatiy, M. A.; Weisberg, O.; Joannopoulos, J. D.; Fink, Y. Perturbation theory for Maxwell's equations with shifting material boundaries. *Phys. Rev. E* **2002**, *65*, 066611.